

Shape-engineerable and highly densely packed single-walled carbon nanotubes and their application as super-capacitor electrodes

DON N. FUTABA^{1,2,3}, KENJI HATA^{1,2*}, TAKEO YAMADA^{1,2}, TATSUKI HIRAOKA^{1,2}, YUHEI HAYAMIZU^{1,2}, YOZO KAKUDATE², OSAMU TANAIKE², HIROAKI HATORI², MOTOO YUMURA^{1,2} AND SUMIO IIJIMA^{1,2}

¹Research Center for Advanced Carbon Materials, Tsukuba 305-8565, Japan

²National Institute of Advanced Industrial Science and Technology (AIST), Tsukuba 305-8565, Japan

³Japan Fine Ceramics Center, National Institute of Advanced Industrial Science and Technology (AIST), Tsukuba 305-8565, Japan

*e-mail: kenji-hata@aist.go.jp

Published online: 26 November 2006; doi:10.1038/nmat1782

We present a rational and general method to fabricate a high-densely packed and aligned single-walled carbon-nanotube (SWNT) material by using the zipping effect of liquids to draw tubes together. This bulk carbon-nanotube material retains the intrinsic properties of individual SWNTs, such as high surface area, flexibility and electrical conductivity. By controlling the fabrication process, it is possible to fabricate a wide range of solids in numerous shapes and structures. This dense SWNT material is advantageous for numerous applications, and here we demonstrate its use as flexible heaters as well as supercapacitor electrodes for compact energy-storage devices.

A carbon nanotube (CNT) possesses excellent electrical^{1–3}, thermal^{4–6} and mechanical^{7–9} properties; however, macroscopic forms of CNTs lose the intrinsic properties of individual CNTs. To address this matter, various CNT forms have been demonstrated ranging through fibres^{10–14}, yarns^{15,16}, mats¹⁷, vertically aligned CNTs (forests)^{18–21}, powders, pellets, foams²² and sheets²³. Each form has unique functionality, for example fibres and yarns are highly durable^{10–16}, CNT pellets are highly dense and forests have a high surface area. Yet, it is difficult to simultaneously retain the fundamental single-walled carbon-nanotube (SWNT) properties, such as high surface area and electrical conductivity, on a macroscopic scale, and have versatility in creating different shapes. This stems from the fabrication processes, which can either damage the tubes or are unable to control the configuration of the tubes within the forms, or both. For example, pellets are brittle, forests are fragile and fibres, yarns and sheets are limited to a single shape.

Here, we present a new macroscopic bulk form of CNT material, which we call the ‘SWNT solid’, in which aligned SWNTs are densely packed while retaining the intrinsic properties of SWNTs, such as high surface area, flexibility and electrical conductivity. Importantly, the shape is engineerable by controlling the fabrication process, which is beneficial for applications spanning from 100% binder-free SWNT electrodes for capacitors to flexible heaters.

Our approach to fabricate high-density SWNT bulk solid exploits a liquid-induced collapse of SWNT forests (Fig. 1a). Previous reports of liquid-induced densification of CNT material have shown interesting morphologies formed from vertically aligned multiwalled carbon-nanotube (MWNT) material or used to strengthen and stiffen bucky paper or aligned MWNT sheets^{23–31}. Most of these reports used relatively short (1–60 µm) MWNT

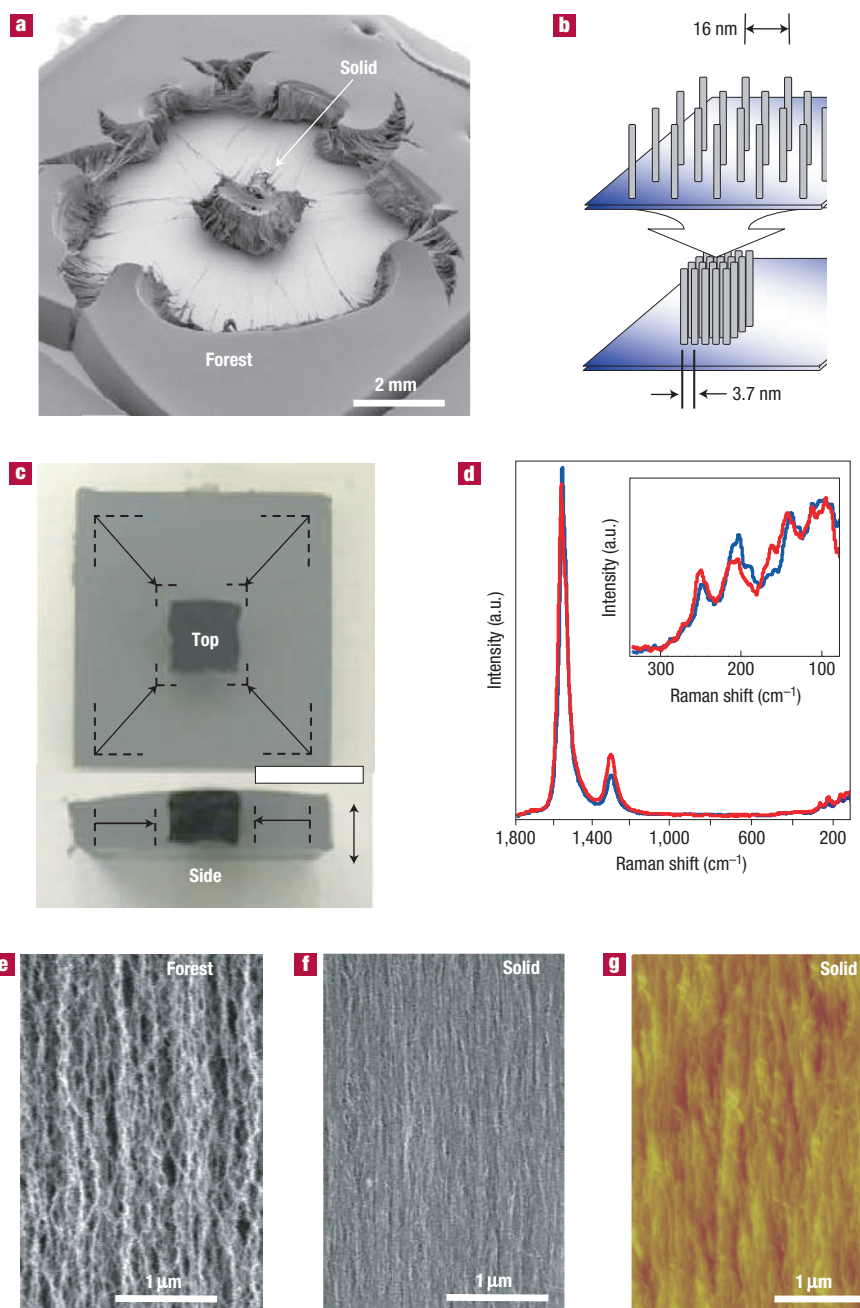


Figure 1 Liquid-induced collapse. **a**, SEM image of SWNT-forest structural collapse from a single drop of liquid. **b**, Schematic diagram of the collapse of the aligned low-density as-grown forest (above) to the highly densely packed SWNT solid (below). **c**, Overlaid pictures illustrating the decrease in lateral dimensions before (grey) and after (black) collapse. The double-ended arrow indicates the tube alignment direction. Scale bar, 1 cm. **d**, Raman spectra for as-grown forest (blue) and SWNT solid (red). **e**, **f**, SEM images of the as-grown forest (**e**) and solid (**f**). **g**, Atomic force microscope image of solid surface.

forests still bound to the catalyst surface. As a result, pyramid-like structures and cellular networks were observed, which resulted from a combination of the tube length, stiffness and surface adhesion. The important difference in this work is the use of long (millimetre-scale) vertically aligned SWNTs that are removed from the substrate as a single unit, uniformly densified and engineered into basic shapes. As-grown SWNT forests are available by advanced high-yield chemical vapour deposition growth, such as water-assisted²¹, alcohol²⁰ and remote-plasma chemical vapour deposition³², of which water-assisted chemical vapour deposition

was used here. For forests used in this research, the typical mass density was 0.03 g cm^{-3} , where 97% is empty space and the average SWNT diameter is 2.8 nm (ref. 33).

When liquids are introduced into the sparse as-grown SWNT forest and dried, the surface tension of the liquids and the strong van der Waals interactions effectively 'zip' the SWNTs together to near-ideal graphitic spacing (Fig. 1b and Supplementary Information Movie S1). This packing occurs in two steps: liquid immersion and evaporation. In the first step, the tubes are drawn together through liquid capillary forces and the forest decreases

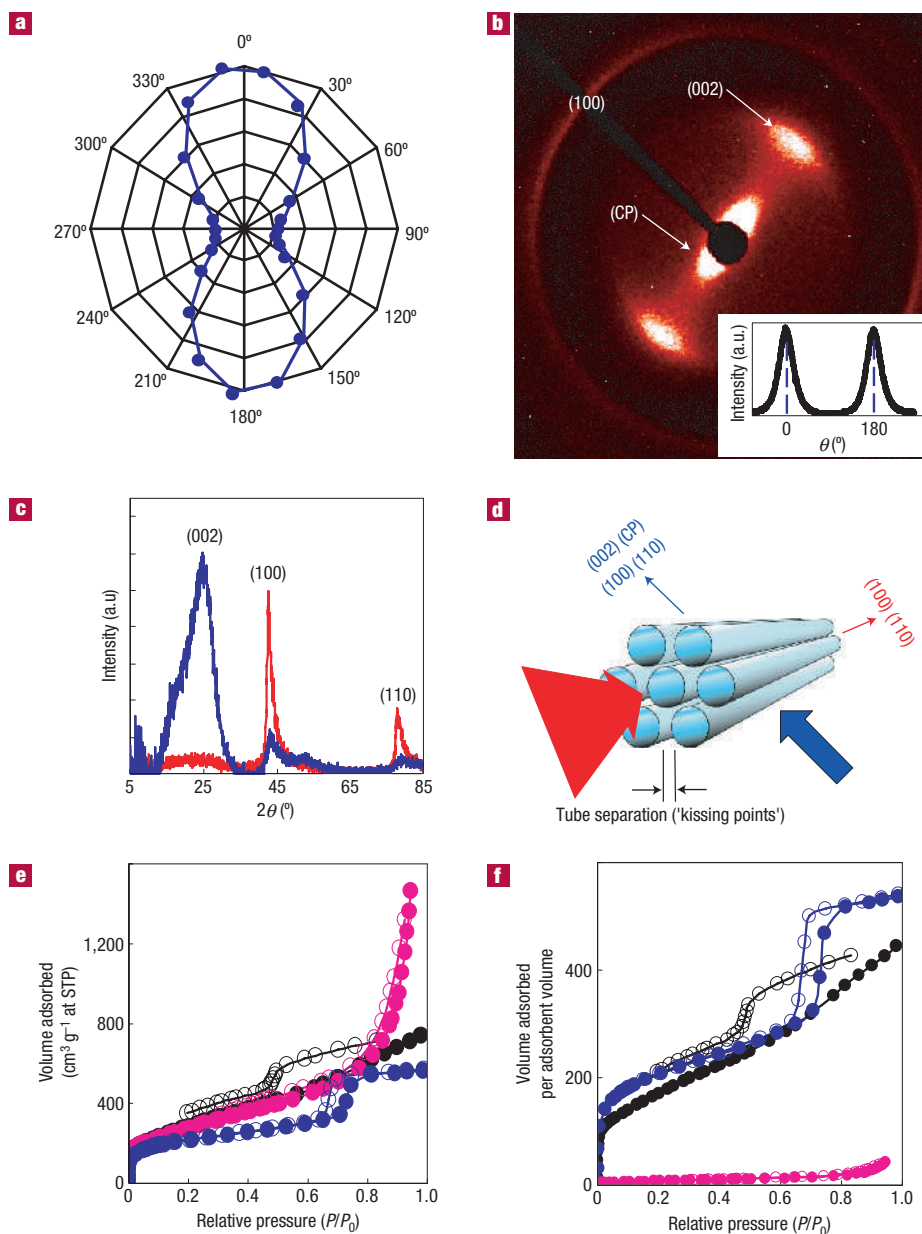


Figure 2 SWNT solid properties. **a**, Optical anisotropy in the graphic 'G'-band by polarized Raman spectroscopy. **b**, Two-dimensional X-ray diffraction image normal to the nanotube axis, showing the anisotropy of the (002) and close-packing peak (CP). Inset: Intensity profile at fixed 2θ as a function of θ for the CP peak. **c**, θ - 2θ X-ray diffraction profiles for two incident beam directions, perpendicular (blue) and parallel (red) to the tube alignment. **d**, Schematic illustration describing the two incident beam directions against a solid. The (002) peak arises from 'kissing points' between neighbouring SWNTs, thus an aligned sample is expected to exhibit a strong signal for normal incidence, whereas the (100) and (110) peaks both originate from the graphitic structure and would be dominant for parallel incidence. **e**, Adsorption (filled circles) and desorption (open circles) isotherms for N_2 at 77 K for SWNT solid (black), SBA-15 (blue) and as-grown forest (pink). **f**, Volumetric adsorption (filled circles) and desorption (open circles) isotherms for N_2 at 77 K for SWNT solid (black), SBA-15 (blue) and as-grown forest (pink).

by $\sim 20\%$ in lateral dimension. On liquid evaporation, van der Waals forces adhere the tubes near to ideal packing, transforming a forest into a small and rigid single body as demonstrated in Fig. 1a, where a 1×1 cm as-grown SWNT forest was contacted by a drop of water in the middle and dried. With no controls, the contacted region collapsed into a compact unit consisting of the tubes initially present in the resultant void. Collapses were observed with all tested liquids, including water, alcohols, acetone, hexane, cyclohexane, dimethylformamide, liquid nitrogen, dioctyl ether, oleic acid and

several machine oils, demonstrating the generality of this approach. Liquid-induced collapse shows a 4.5-fold decrease in the two lateral dimensions but no detectable change in the height, producing a ~ 20 -fold increase in mass density (Fig. 1c). This indicates that alignment of the as-grown forest is critical in triggering efficient liquid-induced collapse (Fig. 1b), an understandable point because the aligned nature provides an ideal condition for optimum van der Waals overlap, leading to well-ordered packing of tubes and structural soundness. Unlike the case in Fig. 1a, the as-grown

Table 1 Comparative summary of structural and physical characteristics

Characteristic	As grown	Solid	Ideal 2.8 nm solid
Density (g cm^{-3})	0.029	0.57	0.78
Tube density (tubes cm^{-2})	4.3×10^{11}	8.3×10^{12}	1.1×10^{13}
Area per tube (nm^2)	234	11.9	8.7
Lattice constant (nm)	16.4	3.7	3.2
SWNT volume occupancy (%)	~2.6	52	72
Vickers hardness	~0.1	7–10	—

forest material was removed from the substrate and completely immersed into a liquid to provide uniform collapse. Significantly, liquid-induced collapse is controllable to fabricate macroscopic-size single-body SWNT solids as demonstrated here and in the following, a feature substantially different from the sponge-like foams made from liquid collapse of MWNTs^{26–29}. Furthermore, the zipping action proceeds without damaging the tubes, as shown by the almost identical Raman spectra (Fig. 1d) before and after collapse. We failed to fabricate such undistorted solids by hydrostatic pressure without inducing damage to the tubes (see Supplementary Information, Figs S1,S2).

Characterization demonstrates that the SWNTs are high-densely packed. Scanning electron microscope (SEM) images of forest (Fig. 1e) and SWNT-solid (Fig. 1f) surfaces (side-view) show marked differences in the apparent density, where numerous inter-tube gaps in forests are not observed. The density is such as to allow atomic force microscopy imaging, showing a smooth and highly uniform surface without gaps (Fig. 1g). By direct mass and size measurements, the density was roughly estimated to be 0.55 g cm^{-3} . An independent estimation measuring the attenuation of a normally incident X-ray beam found the density to be 0.57 g cm^{-3} . These numbers are comparable to that of activated carbon. The lattice constant of the solid material (that is, the distance between axes of adjacent tubes, assuming a two-dimensional hexagonal packing model) was determined to be 3.7 nm from the mass density and mean tube diameter of 2.8 nm (Fig. 2d). This represents a tube-to-tube spacing of 0.9 nm and 72% ideal packing when compared with ideally packed 2.8 nm SWNTs with graphitic spacing of 0.34 nm. SWNT number density was calculated as $8.3 \times 10^{12} \text{ tubes cm}^{-2}$, and the initial 97% empty space in forests reduced to ~50%. The inter-tube and inner-tube volumes are equivalent. The Vickers hardness of the SWNT solid increases over 70-fold to 7–10, which is comparable to that of highly oriented pyrolytic graphite (physical characterizations are summarized in Table 1). The above characterization highlights the solidness and unity of the liquid-induced collapsed material, and thus we call this form an SWNT 'solid'.

SWNT-alignment characterization in the solid with polarized Raman spectroscopy (Fig. 2a) showed a 6.8 optical anisotropy ratio of the graphitic 'G'-band intensity (strongest when parallel to the alignment direction), which is comparable to or higher than other aligned CNT forms^{34,35} and identical to the as-grown forest. Two-dimensional X-ray diffraction (XRD) on a 250- μm -wide, 550- μm -tall solid sample (Fig. 2b) showed anisotropy of the (002) and the close-packed (CP) peaks (see the Supplementary Information). Although unobservable for an individual SWNT, the (002) arises from the 'kissing' of adjacent SWNTs in a collection of SWNTs. The relatively broad (002) reflection is centred at $2\theta = 25.5^\circ$, which corresponds to a d spacing of 0.35 nm (consistent with graphitically spaced CNTs). The broadness of the peak reflects the imperfect long-range order of the SWNT sample. Statistically, isotropic alignment would result in a circular (002) appearance; therefore, the observed strong anisotropy indicates significant

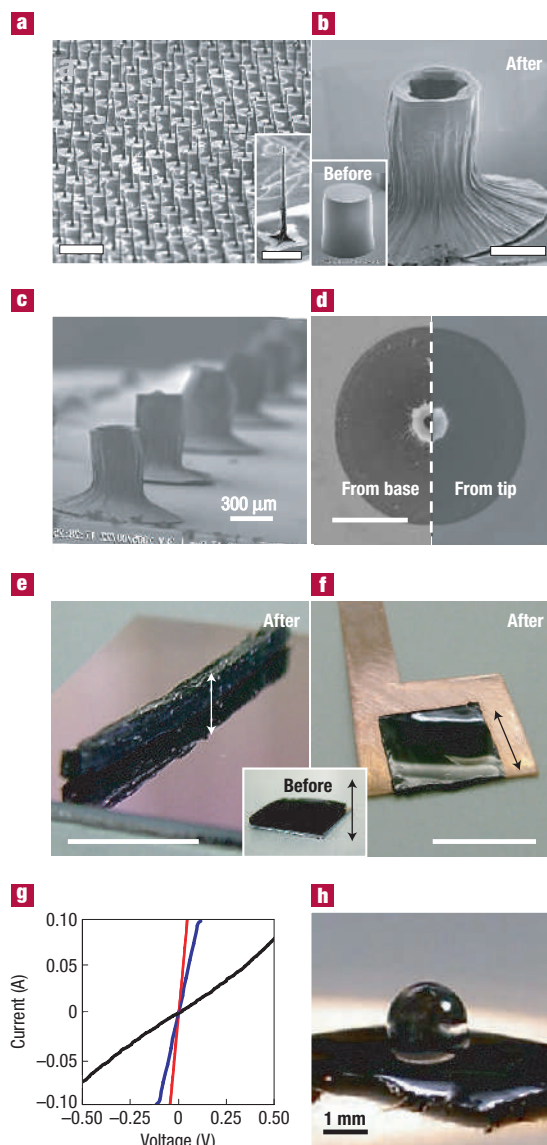


Figure 3 Engineerable shape. **a**, SEM image of an array of lithographically designed solid needles. Scale bar, 100 μm . Inset: Magnified individual needle. Scale bar, 60 μm . **b**, SEM image of a 'microvolcano'. Scale bar, 250 μm . Inset: 'Microvolcano' before collapse. **c**, Array of 'microvolcano' structures. Scale bar 300 μm . **d**, Split SEM image of base (left) and tip (right) liquid contact. Scale bar, 200 μm . **e**, SWNT solid engineered into a rigid 'bar'. Scale bar, 1 cm. Inset: Photograph of the as-grown forest. **f**, Flexible SWNT solid engineered into a flattened sheet adhered to a copper sheet. Scale bar, 1 cm. **g**, I - V characteristics of the SWNT solid sheet (blue), pressed as-grown SWNT forest (black) and copper (red). **h**, Water droplet on SWNT solid sheet surface. Scale bar 1 mm. In **e** and **f** the double-ended arrows indicate tube alignment.

alignment. Order-parameter determination^{36,37} of the (002) peak profile gave a value of 0.72, which quantitatively illustrates the uniform alignment of the 'kissing points' throughout the sample. θ - 2θ XRD measurement on a 1 mm² sample similarly showed strong anisotropies in the (002), (100) and (110) peaks (Fig. 2c,d). Whereas the CP and (002) peaks arise from the dense packing, the (100) and (110) peaks originate from the graphene character of the CNTs. In addition, the CP peak profile (Fig. 2b, inset) was clearly

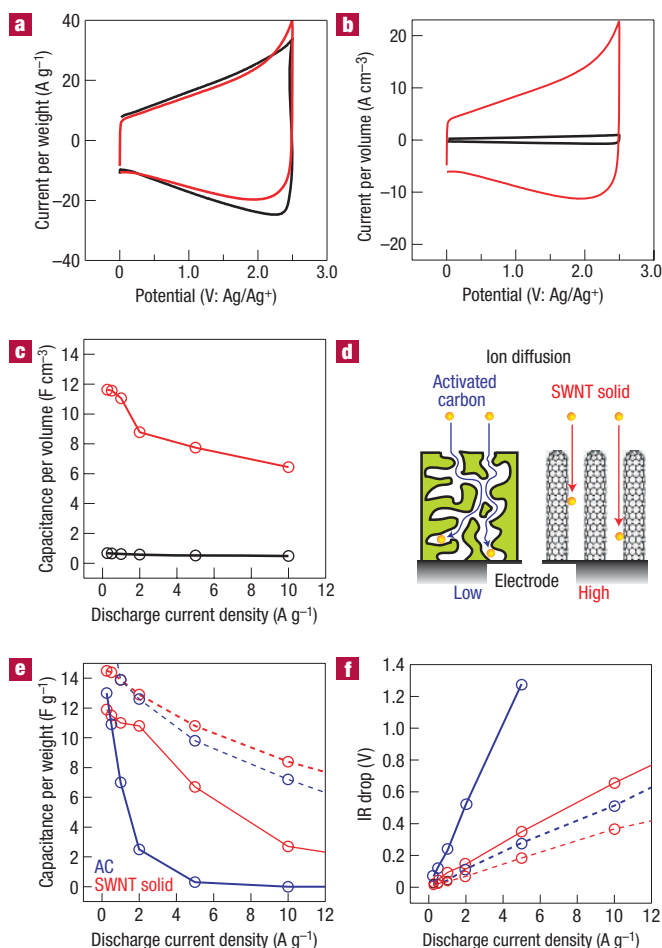


Figure 4 Applications. **a,b**, Cyclic voltammograms of the EDLC using the SWNT solid sheet (red) and as-grown forest (black) as electrodes comparing the capacitance per weight (**a**) and capacitance per volume (**b**). **c**, Change in the capacitance per volume using the SWNT solid sheet (red) and as-grown forest (black). **d**, Schematic model comparing the ion diffusion for activated carbon and the SWNT solid material. **e**, Capacitance versus discharge current density comparing SWNT solid (red) and activated carbon (blue) for 0.1 and 0.5 mm electrode thicknesses (dashed and solid lines, respectively). **f**, Potential drop associated with an increase in internal resistance (IR drop) for SWNT solid (red) and activated carbon (blue) for 0.1 and 0.5 mm electrode thicknesses (dashed and solid lines, respectively).

observable, from which the order parameter was determined to be 0.62. This value is particularly encouraging, because the anisotropy of the peak is weakened from the broad diameter distribution (see the Supplementary Information), and therefore we consider this a lower limit for the CP order parameter. These results confirm long-range bulk alignment throughout the solid, a matter of importance in exploiting the true one-dimensional nature of CNTs in real applications. This anisotropy would not be observable in a truly isotropic collection of CNTs, such as a macroscopic aggregation of bundles.

Significantly, the SWNT solid possesses a high surface area almost identical to the as-grown forest despite the highly dense packing of SWNTs, meaning a considerable increase in the volumetric adsorption density, an indicator of surface area per unit volume. The estimated Brunauer–Emmett–Teller (BET) surface

area for the solid, as determined from nitrogen adsorption isotherms (Fig. 2e), was $1,000\text{ m}^2\text{ g}^{-1}$, being similar to that of as-grown SWNTs. Despite the dramatically decreased inter-tube spacing, the average tube separation ($\sim 0.9\text{ nm}$) is sufficient to allow for full monolayer coverage on adjacent nanotubes, thus retaining its surface area (see the Supplementary Information, Fig. S3). These surface-area values are much higher than that measured for closed HiPco samples ($520\text{ m}^2\text{ g}^{-1}$ (ref. 38)). The volumetric adsorption density jumps 20-fold compared with the as-grown forest (Fig. 2f). Furthermore, SWNT solids have a comparable or superior surface area and volumetric adsorption density to SBA-15, a standard mesoporous silica material^{39–41}, with the additional advantage of consisting of a single unit rather than micrometre-sized grains.

The SWNT-solid concept can be extended to create a variety of unique solid structures from as-grown forest material with diverse shapes by controlling parameters that influence the collapse process, such as forest aspect ratio, initial liquid contact point and substrate–forest interaction. For example, lithographically defined as-grown SWNT circular pillars²¹ with high aspect ratio collapsed from the tip create well-defined and patterned SWNT solid needles with high aspect ratio (Fig. 3a and inset). In contrast, low-aspect-ratio SWNT circular pillars (Fig. 3b, inset) with strong substrate interaction collapsed from the surface edge result in a vastly different structure, resembling a ‘microvolcano’ (Fig. 3b,c). The peripheral collapse draws nanotubes radially outward from within the pillars, thus creating a cavity. Figure 3d is a split image, showing the result of liquid contact from the base (creating a volcano) or from the tip (creating a closed stalagmite-like structure). These two examples illustrate how the collapse process can be manipulated to design unique high-density SWNT structures possessing the benefit of being both mechanically and electrically durable.

Another approach to extend our ability to engineer the shape of the solid is to use moderate external forces, such as very light pressure, to direct the direction of the collapse. For example, applying light pressure in one lateral direction suppresses collapse in one lateral dimension and creates a bar (Fig. 3e). Similar application of light pressure at a shearing angle to the alignment induces a vertical collapse, without any collapse in either of the lateral dimensions, which results in a solid sheet (Fig. 3f). A clip is enough to direct the collapse process (see the Supplementary Information, Fig. S4). Because the SWNTs are directed to lie flat; the solid sheets maintain a comparable degree of alignment of the forest, and the direction of alignment is controllable by changing the direction of pressure. This approach is easily extendable to fabricate strongly adhered solid sheets on desired flat substrates without the use of bonding agents by simply transferring the forest onto a target substrate and implementing the collapse process. Figure 3f shows an example of a 1 mm tall, $1 \times 1\text{ cm}$ forest collapsed into a $1 \times 1\text{ cm}$, optically flat solid sheet with a height less than $100\mu\text{m}$ strongly adhered on a copper contact, a form useful for multiple applications, for example an ideal 100% binder-free SWNT electrode for supercapacitors. Moreover, advanced control of the shape is possible by combining lateral and vertical collapse to fabricate solids with arbitrary dimensions; for example, it is possible to generate a solid sheet with a height of $500\mu\text{m}$ but with smaller lateral size from the same forest as mentioned above. Note that the applied pressure is extremely weak, and thus does not damage the SWNTs, as shown by the almost identical Raman spectra of the solids and forests (see the Supplementary Information, Fig. S1). The ability to engineer the shapes of solids is beneficial for a multitude of applications requiring high-surface-area, high-density, aligned, conducting and flexible or rigid CNT material, as demonstrated in the following.

Whereas the SWNT solid in a bulk form, as seen in Fig. 1c, exhibits brittle behaviour just as in other bulk forms of CNTs,

the engineered solid in the form of an aligned sheet showed no observable change in conductivity as the radius of curvature was reduced below 100 μm (see the Supplementary Information, Fig. S5) and showed exceptional non-brittle behaviour when the radius of curvature was reduced below 35 μm (see the Supplementary Information, Fig. S5).

The conductivity of the solid sheets was examined on samples where a 1×1 cm solid sheet with 100 μm height was sandwiched between metal contacts, and compared with the conductivity of forests pressed with the same pressure without liquid and copper sheets attached together (Fig. 3g). The I - V characteristics of the solid sheet show ohmic behaviour with resistance less than 1 Ω . Measurements clearly show superior conductance of solid sheets compared with pressed forests, highlighting the importance of liquid-induced high-density packing. Four-point resistance measurements of 50- μm -thick aligned SWNT solid sheets both parallel and perpendicular to the alignment direction showed sheet resistances of 1.74 and 2.61 Ω per square, respectively. Curiously, the electronic anisotropy is less than the measured structural anisotropy, a point that requires future efforts to clarify. Furthermore, whereas the SWNT solid in Fig. 1a was made from forest immersed into water, once collapsed the solid exhibits an entirely different affinity towards water (Fig. 3h). A water droplet on the solid made a high contact angle ($> 140^\circ$) and did not infuse before evaporating, highlighting the difference between SWNT solid and as-grown forest.

To demonstrate the use of the flexibility and conductivity of solid sheets, we made a flexible heater from a patterned solid sheet coated with a polyimide film (see the Supplementary Information, Fig. S6). The effective resistance was increased to 1.5 k Ω by lengthening the heating element through a zigzag pattern and by aligning the nanotubes perpendicular to the zigzag direction. The heater delivered power in excess of 15 W for over 60 min without degradation and could boil water in less than 5 min (see the Supplementary Information, Movie S2).

Having a high surface area in a small volume is desirable for compact energy storage. Because of their high surface area, excellent conductivity and crystallinity, SWNTs are potential candidates as electrodes for supercapacitors⁴². To demonstrate the potential of the SWNT solid in this direction, we constructed two-electrode electric double-layer capacitor (EDLC) cells with solid sheets and forests (for comparison) as the active materials with tetraethylammonium tetrafluoroborate (Et_4NBF_4)/propylene carbonate electrolyte and measured their electrochemical properties. The respective SWNT materials were sandwiched between Pt sheets (current collector) and Pt meshes. As the drying process is crucial to the densification process, no significant electrolyte-driven densification of the SWNT forests was observed. Conversely, occasionally a slight expansion of the SWNT solid was observed, particularly when operated at high voltages. In these systems, the capacitance of the cell can be estimated from the enclosed volume of the cyclic voltammograms. Cyclic voltammograms of the solid sheet and forest cells (Fig. 4a) were very similar, meaning the two materials have nearly the same capacitance per weight (difference $\sim 15\%$), and also correspond to the similar BET surface areas discussed earlier. Considering the density difference of these two materials, capacitors using SWNT solid electrodes have a significantly higher capacitance per volume, as shown in Fig. 4b. This aspect is vital for the use of supercapacitors in confined spaces, for example, mobile phones. The capacitance of the SWNT solid EDLC was estimated as 20 F g^{-1} from the discharge curves of cells charged at 2.5 V for a two-electrode cell, and corresponds to 80 F g^{-1} for a three-electrode cell. This is roughly twice the capacitance of 45 F g^{-1} reported for HiPco SWNT three-electrode cells, and agrees with the difference in

their BET surface areas. The energy density ($W = CV^2/2$) was estimated to be 69.4 Wh kg^{-1} (from 80 F g^{-1}) when normalized to the single electrode weight, which is higher than those of CNT-based supercapacitors previously reported by Niu *et al.*⁴³ (approximately 0.5 Wh kg^{-1}), Du *et al.*⁴⁴ (11 Wh kg^{-1}) and Xu *et al.*⁴⁵ (49 Wh kg^{-1}).

We further illustrate that SWNT solids serve as excellent electrodes for compact high-power-density cells. To this end, we studied the rate performance of SWNT solid and SWNT forest cells shown in Fig. 4c as plots of capacitances per volume versus the discharge current density. These plots show the capacitance decrease at increased power operation (high discharge current density). Whereas the SWNT solid EDLC consistently exhibited a higher capacitance per volume at increased power operation than its as-grown counterpart, the capacitance per volume of the SWNT solid gradually decreased with increased operating power (the as-grown EDLC showed little change). Because the electrolyte ions must diffuse through the pores of interstitial regions within the SWNT packing structure (Fig. 4d), ion accessibility is limited in the inner region of the solids on the relevant timescale. When operated at high current (high power), ion diffusivity becomes a limiting factor because regions where ions fail to diffuse increase, which results in a decrease in capacitance.

Ion diffusivity plays a key factor to realize compact supercapacitors with high energy density and high power density. To demonstrate these strengths of SWNT solid EDLCs, we built capacitor cells with electrodes with different thicknesses from solid sheets and activated carbon (for comparison). For activated carbon, thicker electrodes possess higher ion diffusion barriers in the inner region of the electrode (Fig. 4d), resulting in higher internal resistance and inferior high-power performance. This factor limits the practical thickness of activated carbon electrodes. In contrast, thick electrodes are advantageous to increase the energy density because in such cells the active material can occupy high ratios of the volume and weight. Thus, ideally a thick electrode that both possesses high capacitance and is operable at high power is desired. From the discharge curves, the capacitances normalized to a single electrode weight and the potential drop associated with an increase in internal resistance of SWNT solid and activated carbon cells with electrodes with two different thicknesses (100 and 500 μm) were estimated, and their dependences on discharge current density (operating power) were plotted (Fig. 4e,f, respectively). Generally, cells with thicker electrodes showed inferior performance, such as increase of the internal resistances and smaller capacitances at high current. When compared with activated carbon cells, the SWNT solid cells showed higher capacitance, less capacitance drop at high power operation and better performance for thick electrodes. The superior characteristics of SWNT solid cells are highlighted by the performance difference in 500- μm -thick electrodes, where the activated-carbon-based electrode failed to operate as a capacitor. Superior electrochemical properties of solid sheets originate from better ion diffusivity of aligned SWNT material than activated carbon. We believe the superior ion diffusivity of SWNT solids stems from the aligned pore structures compared with activated carbon (Fig. 4d). From the potential drop associated with an increase in internal resistance of Fig. 4f, the maximum power density of the electrodes of SWNT solid and activated carbon cells (thickness 100 μm /500 μm) were calculated as 43.3 kW kg^{-1} /24 kW kg^{-1} and 31.2 kW kg^{-1} /12 kW kg^{-1} , respectively. Despite the use of thicker electrode material, the power densities for the SWNT solid capacitor were higher than or comparable to those for previously reported CNT-based supercapacitors that use an electrolyte solution of higher ion conductivity^{43,44}. Taken together, these results demonstrate that the SWNT solid is an excellent material for compact, high-power

delivery and high-energy-density storage, and we believe that it would be an ideal candidate for the active material of next-generation supercapacitors.

In summary, our studies have outlined a general and rational strategy to fabricate an aligned high-densely packed SWNT solid material by using the zipping effect of liquids to draw nanotubes together. These studies represent substantial progress towards producing macroscopic-scale high-density SWNT material engineered in both shape and structure, opening diverse functionality that is advantageous for numerous applications, such as energy storage. Our approach is unique from other existing processes to make CNT forms, for example those that use dispersion solutions, because the nanotubes are not harmed and thus the properties of SWNTs are retained in the macroscopic-scale material. By using various techniques to assist the collapse process, it is possible to fabricate a variety of solids spanning rods, needles and sheets. We believe that our approach can be extended further to make new and sophisticated CNT forms by using more complex SWNT forests or introducing different materials into the system. Future work on the basis of the synthesis of SWNT forest on metal foils⁴⁶ should open the possibility for the continuous growth of SWNT forests and provide a scalable route for fabricating continuous solid sheets. These advances may extend the frontier of CNT research and open up new paths to accelerate development of applications.

METHODS

SYNTHESIS

SWNTs were synthesized in a 1 inch tube furnace by water-assisted chemical vapour deposition²¹, 'supergrowth' at 750 °C with a C₂H₄ carbon source and an Al₂O₃ (10 nm)/Fe (1 nm) thin-film catalyst on silicon wafers. We used He with H₂ as the carrier gas (total flow 1,000 standard cubic centimetres per minute (s.c.c.m.)) at 1 atm with a controlled amount of water vapour (concentration 100 p.p.m. to 150 p.p.m.). Growth was performed at 750 °C with ethylene (100 s.c.c.m.) for 10 min.

LIQUID-INDUCED SWNT-FOREST COLLAPSE

We typically carried out collapse of as-grown forests using a highly diluted ethyl alcohol solution. Depending on the desired purpose, we removed forests from the catalytic surfaces and placed them into a small beaker containing the alcohol solution, where the collapse process began. As the liquid enters the inter-tube regions, a noticeable decrease in the physical dimensions occurs, after which the forests sink. At that time, we remove them from the solution and allow them to dry on a clean silicon surface, where the final stage of the collapse occurs.

RAMAN SPECTROSCOPY

Raman spectroscopy was done using a thermo-electron Raman spectrometer with 532 nm excitation wavelength.

HARDNESS MEASUREMENT

We used a Matsuzawa Seiki microhardness tester ($\mu = 0.001$ mm) with loads ranging from 10 to 100 g and a dwell time of 10–30 s. Hardness testing both parallel and perpendicular to the nanotube alignment direction showed little difference, yet as expected the high-densely packed SWNT material showed much higher elastic compliance perpendicular to the alignment.

X-RAY DIFFRACTION

Two-dimensional XRD imaging was carried out on a Bruker SMART CCD (charge-coupled device) area-detector diffractometer (rotating unit) using a Mo-K α X-ray source (0.71073 Å) at a total power of 4.5 kW. The sample-detector distance was 5.968 cm and the CCD detector has dimensions of 6.1 × 6.1 cm. During measurement, we rotated the cylindrically symmetric sample about its symmetry axis during data acquisition.

We carried out θ – 2θ XRD using a Rigaku X-ray diffractometer with a Cu-K α X-ray source at a total power of 15 kW. We used solid samples in the shape of a rectangular parallelepiped with the dimensions 1 × 1 × ~2.4 mm, with the alignment direction along one of the short-dimension directions. We

affixed the sample to a mount to allow for rotation about its long axis. Small-angle XRD scans exhibited a broad peak corresponding to a d spacing of 4.4 nm, which we suspect corresponds loosely to the close packing of the SWNTs. With the detector fixed at this 2θ position, we measured the intensity profile as the sample was rotated about its axis θ (Fig. 2b, inset).

Order-parameter determination was made using a standard formulation, as defined by

$$f \equiv \frac{1}{2} (3 \langle \cos^2 \theta \rangle - 1)$$

$$\text{where } \langle \cos^2 \theta \rangle = \frac{\int_0^{\pi/2} I(\theta) \cos^2 \theta \sin \theta d\theta}{\int_0^{\pi/2} I(\theta) \sin \theta d\theta},$$

I is the signal intensity as a function of θ and θ is the angle between the structural unit vector and the reference direction^{35,36}.

DENSITY DETERMINATION

We estimated the density by attenuation of a normally incident 500- μ m-diameter X-ray beam, following the relation $I_x = I_0 e^{-(\mu/\rho) \rho x}$, where I_x is the transmitted X-ray intensity through a distance x , I_0 is the incident intensity, x is the thickness of the sample; we define μ/ρ as the mass absorption coefficient, which is a constant of the material and independent of the physical state, and ρ is the mass density. The value for μ/ρ was determined by X-ray attenuation through a highly oriented pyrolytic graphite sample of known density and thickness and was similar to values found in the literature⁴⁷.

SURFACE-AREA MEASUREMENT

The BET surface area was estimated from nitrogen adsorption isotherms at 77 K for 50 mg SWNT solid samples using a BEL Japan: BELSORP Mini II surface-area and pore-size analysis system.

CYCLIC VOLTAMMETRY

After vacuum heating of the SWNT material, we assembled the two-electrode supercapacitors on a Pt current collector in a dry argon environment by sandwiching two SWNT solid-sheet samples separated by a non-conducting porous glass filter and immersed into a 1 M Et₄NBF₄/propylene carbonate electrolyte (Tomiyama Pure Chemical). We obtained electrochemical characteristics of the solid-sheet-material electrodes by cyclic voltammetry (1 mV s^{−1}) from 0 to 2.5 V (VMP2, Princeton Applied Research) and by galvanostatic charge/discharge (50–20,000 mA g^{−1}).

We used commercially available activated carbons for the EDLC, YP17 (Kuraray), for comparison. We prepared the electrode sheets of YP17 with the thickness of approximately 100 μ m by mixing and kneading with 10 wt% Teflon binder and carbon black and then hot-pressing on a Pt current collector.

Received 2 June 2006; accepted 13 October 2006; published 26 November 2006.

References

- Frank, S. P., Poncharal, P., Wang, Z. L. & de Heer, W. A. Carbon nanotube quantum resistors. *Science* **280**, 1744–1746 (1998).
- Liang, W. *et al.* Fabry–Perot interference in a nanotube electron waveguide. *Nature* **411**, 665–669 (2001).
- Baughman, R. H., Zakhidov, A. A. & de Heer, W. A. Carbon nanotubes—the route toward applications. *Science* **297**, 787–792 (2002).
- Kim, P., Shi, L., Majumdar, A. & McEuen, P. L. Thermal transport measurements of individual multiwalled nanotubes. *Phys. Rev. Lett.* **87**, 215502 (2001).
- Kociak, M. *et al.* Superconductivity in ropes of single-walled carbon nanotubes. *Phys. Rev. Lett.* **86**, 2416–2419 (2001).
- Tang, Z. K. *et al.* Superconductivity in 4 Å single-walled carbon nanotubes. *Science* **292**, 2462–2465 (2001).
- Wong, E. W., Sheehan, P. E. & Lieber, C. M. Nanobeam mechanics: Elasticity, strength, and toughness of nanorods and nanotubes. *Science* **277**, 1971–1975 (1997).
- Walters, D. A. *et al.* Elastic strain of freely suspended single-walled carbon nanotube ropes. *Appl. Phys. Lett.* **74**, 3803–3805 (1999).
- Yu, M.-F., Files, B. S., Arepalli, S. & Ruoff, R. S. Tensile loading of ropes of single wall carbon nanotubes and their mechanical properties. *Phys. Rev. Lett.* **84**, 5552–5555 (2000).
- Thess, A. *et al.* Crystalline ropes of metallic carbon nanotubes. *Science* **273**, 483–487 (1996).
- Vigolo, B. *et al.* Macroscopic fibers and ribbon of oriented carbon nanotubes. *Science* **290**, 1331–1334 (2000).
- Zhu, H. W. *et al.* Direct synthesis of long single-walled carbon nanotube strands. *Science* **296**, 884–886 (2002).
- Ericson, L. M. *et al.* Macroscopic, neat, single-walled carbon nanotube fibers. *Science* **305**, 1447–1450 (2004).
- Li, Y., Kinloch, I. A. & Windle, A. H. Direct spinning of carbon nanotube fibers from chemical vapor deposition synthesis. *Science* **304**, 276–278 (2004).
- Jiang, K., Li, Q. & Fan, S. Spinning continuous carbon nanotube yarns. *Nature* **419**, 801 (2002).

16. Zhang, M. *et al.* Multifunctional carbon nanotube yarns by downsizing an ancient technology. *Science* **306**, 1358–1361 (2004).
17. Rinzler, A. G. *et al.* Large-scale purification of single-wall carbon nanotubes: Process, product, and characterization. *Appl. Phys. A* **67**, 29–37 (1998).
18. Ren, Z. F. *et al.* Synthesis of large arrays of well-aligned carbon nanotubes on glass. *Science* **282**, 1105–1107 (1998).
19. Fan, S. *et al.* Self-oriented regular arrays of carbon nanotubes and their field emission properties. *Science* **283**, 512–514 (1999).
20. Murakami, Y. *et al.* Growth of vertically aligned single-walled carbon nanotube films on quartz substrates and their optical anisotropy. *Chem. Phys. Lett.* **385**, 298–303 (2004).
21. Hata, K. *et al.* Water-assisted highly efficient synthesis of impurity-free single-walled carbon nanotubes. *Science* **306**, 1362–1364 (2004).
22. Cao, A., Dickrell, P. L., Sawyer, W. G., Ghasemi-Nejhad, M. N. & Ajayan, P. M. Super compressible foamlike carbon nanotube films. *Science* **310**, 1307–1310 (2005).
23. Zhang, M. *et al.* Strong, transparent, multifunctional, carbon nanotube sheets. *Science* **309**, 1215–1219 (2005).
24. Nguyen, C. V. *et al.* Preparation of nucleic acid functionalized carbon nanotube arrays. *Nano Lett.* **2**, 1079–1081 (2002).
25. Lau, K. K. S. *et al.* Superhydrophobic carbon nanotube forests. *Nano Lett.* **3**, 1701–1705 (2003).
26. Fan, J. G., Dyer, D., Zhang, G. & Zhao, Y.-P. Nanocarpet effect: Pattern formation during the wetting of vertically aligned nanorod arrays. *Nano Lett.* **4**, 2133–2138 (2004).
27. Correa-Duarte, M. A. *et al.* Fabrication and biocompatibility of carbon nanotube-based 3D networks as scaffolds for cell seeding and growth. *Nano Lett.* **4**, 2233–2236 (2004).
28. Liu, H. *et al.* Self-assembly of large-scale micropatterns on aligned carbon nanotube films. *Angew. Chem.* **43**, 1146–1149 (2004).
29. Chakrapani, N., Wei, B., Carrillo, A., Ajayan, P. & Kane, R. S. Capillary-driven assembly of two-dimensional cellular carbon nanotube foams. *Proc. Natl Acad. Sci.* **101**, 4009–4013 (2004).
30. Ko, H., Peleshanko, S. & Tsukruk, V. V. Combining and bending of carbon nanotube arrays with confined microfluidic flow on patterned surfaces. *J. Phys. Chem.* **108**, 4385–4393 (2004).
31. Whitten, P. G., Spinks, G. M. & Wallace, G. G. Mechanical properties of carbon nanotube paper in ionic liquid and aqueous electrolytes. *Carbon* **43**, 1891–1896 (2005).
32. Zhong, G. *et al.* Large-area synthesis of carbon nanofibers by low-power microwave plasma-assisted CVD. *Chem. Vapor Dep.* **10**, 125–128 (2004).
33. Futaba, D. N. *et al.* 84% Catalyst activity of water-assisted growth of single walled carbon nanotube forest characterization by a statistical and macroscopic approach. *J. Phys. Chem. B* **110**, 8035–8038 (2006).
34. Duesberg, G. S., Loa, I., Burghard, M., Syassen, K. & Roth, S. Polarized raman spectroscopy on isolated single-wall carbon nanotubes. *Phys. Rev. Lett.* **85**, 5436–5439 (2000).
35. Murakami, Y. *et al.* Polarization dependence of resonant Raman scattering from vertically aligned single-walled carbon nanotube films. *Phys. Rev. B* **71**, 085403 (2005).
36. Klug, H. & Alexander, L. E. (eds) in *X-ray Diffraction Procedures* 2nd edn (Wiley, New York, 1974).
37. Lovell, R. & Mitchell, G. R. Molecular-orientation distribution derived from an arbitrary reflection. *Acta Crystallogr. A* **37**, 135–137 (1981).
38. Yang, C.-M., Kaneko, K., Yudasaka, M. & Iijima, S. Effect of purification on pore structure of hipco single-walled carbon nanotube aggregates. *Nano Lett.* **2**, 385–388 (2002).
39. Zhao, D. *et al.* Triblock copolymer synthesis of mesoporous silica with periodic 50–300 Angstrom pores. *Science* **279**, 548–552 (1998).
40. Zhao, D. *et al.* Nonionic triblock and star diblock copolymer and oligomeric surfactant synthesis of highly ordered, hydrothermally stable, mesoporous silica structures. *J. Am. Chem. Soc.* **120**, 6024–6036 (1998).
41. Yamada, T., Zhou, H.S., Asai, K. & Honma, I. Pore size controlled mesoporous silicate powder prepared by triblock copolymer templates. *Mater. Lett.* **56**, 93–96 (2002).
42. Shirashi, S., Kurihara, H., Okabe, K., Hulicova, D. & Oya, A. Electric double layer capacitance of highly pure single-walled carbon nanotubes (HiPco™ Buckytubes™) in propylene carbonate electrolytes. *Electrochem. Commun.* **4**, 593–598 (2002).
43. Niu, C., Sichel, E. K., Hoch, R., Moy, D. & Tennent, H. High power electrochemical capacitors based on carbon nanotube electrodes. *Appl. Phys. Lett.* **70**, 1480–1482 (1997).
44. Du, C., Yeh, J. & Pan, N. High power density supercapacitors using locally aligned carbon nanotube electrodes. *Nanotechnology* **16**, 350–353 (2005).
45. Xu, B. *et al.* Room temperature molten salt as electrolyte for carbon nanotube-based electric double layer capacitors. *J. Power Sources* **158**, 773–778 (2006).
46. Hiraoka, T. *et al.* Synthesis of single- and double-walled carbon nanotube forests on conducting metal foils. *J. Am. Chem. Soc.* **128**, 13338–13339 (2006).
47. *International Tables for X-ray Crystallography* Vol. II (Reidel, Boston, MA, 1959 and 1972).

Acknowledgements

We gratefully acknowledge S. Usuba for the use of the microhardness tester and the contributions by T. Namai, M. Mizuno, A. Otsuka, K. Ozawa and S. Yamada. We also gratefully acknowledge M. Goto and K. Nakayama for their discussions and assistance on X-ray diffraction. Partial support by the New Energy and Industrial Technology Development Organization (NEDO) Nano-Carbon Technology project is acknowledged. Correspondence and requests for materials should be addressed to K.H. Supplementary Information accompanies this paper on www.nature.com/naturematerials.

Author contributions

D.N.F. and K.H. conceived and designed the experiments; D.N.F. performed the experiments; T.Y. and T.H. contributed to material analyses; Y.H. contributed to material preparation; T.H., O.T. and H.H. contributed to super-capacitor preparation/characterization; Y.K. contributed XRD analysis tools and D.N.F. and K.H. co-wrote the paper.

Competing financial interests

The authors declare that they have no competing financial interests.

Reprints and permission information is available online at <http://npg.nature.com/reprintsandpermissions/>